J|A|C|S ARTICLES

Published on Web 07/01/2009

Topotactic Reduction As a Route to New Close-Packed Anion Deficient Perovskites: Structure and Magnetism of 4H-$BaMnO_{2+x}$

Joke Hadermann,[†] Artem M. Abakumov,[†] Josephine J. Adkin,[‡] and Michael A. Hayward*[,‡]

EMAT, University of Antwerp, Groenenborgerlaan 171, B-2020 Antwerp, Belgium, and Department of Chemistry, Inorganic Chemistry Laboratory, University of Oxford, South Parks Road, Oxford OX1 3QR, United Kingdom

Received April 22, 2009; E-mail: michael.hayward@chem.ox.ac.uk

Abstract: The anion-deficient perovskite 4H-$BaMnO_{2+x}$ has been obtained by a topotactic reduction, with LiH, of the hexagonal perovskite 4H-$BaMnO_{3-x}$. The crystal structure of 4H-$BaMnO_{2+x}$ was solved using electron diffraction and X-ray powder diffraction and further refined using neutron powder diffraction (S.G. *Pnma*, $a = 10.375(2)$ Å, $b = 9.466(2)$ Å, $c = 11.276(3)$ Å, at 373 K). The orthorhombic superstructure arises from the ordering of oxygen vacancies within a 4H (*chch*) stacking of close packed *c*-type $BaO_{2.5}$ and *h*-type $BaO_{1.5}$ layers. The ordering of the oxygen vacancies transforms the Mn_2O_9 units of face-sharing MnO_6 octahedra into Mn_2O_7 (two corner-sharing tetrahedra) and Mn_2O_6 (two edge-sharing tetrahedra) groups. The Mn_2O_7 and Mn_2O_6 groups are linked by corner-sharing into a three-dimensional framework. The structures of the $BaO_{2.5}$ and $BaO_{1.5}$ layers are different from those observed previously in anion-deficient perovskites providing a new type of order pattern of oxygen atoms and vacancies in close packed structures. Magnetization measurements and neutron diffraction data reveal 4H-$BaMnO_{2+x}$ adopts an antiferromagnetically ordered state below $T_N \approx 350$ K.

Introduction

Complex transition metal oxides have been of longstanding interest due to the wide range of physical properties they exhibit. Much of the complex behavior observed in these phases arises from the strong coupling which exists between the electronic states on neighboring metal centers. This coupling is generally mediated and facilitated by the orbitals of the intervening oxide anions and is therefore strongly influenced by the topology and geometry of the transition metal−oxygen network. In the search for new electronic materials and phenomena, a fruitful approach is to prepare phases with new transition metal−oxygen networks based on metals expected to exhibit strong electronic coupling.

Materials based on the ABO_3 perovskite series of structures have been observed to exhibit exceptionally strong electronic coupling.[1] The structural series can be described with reference to close packed lattices. If one quarter of the oxide ions in a two-dimensional close packed O_4 sheet are replaced in an ordered manner by an "A-cation", to yield layers of stoichiometry AO_3, perovskite structures are generated by stacking these layers in an ordered manner. An ABCA cubic stacking sequence, analogous to that observed in FCC lattices, yields the basis of a 3C (*ccc*) cubic perovskite structure which is completed by the insertion of small B-cations (typically transition metals) into one quarter of the octahedral sites which are formed between adjacent layers of oxygen atoms. Incorporation of some ABA hexagonal stacking into the arrangement of AO_3 layers, analogous to that observed in HCP lattices, allows the formation of an almost unlimited number of structural polytypes referred to as hexagonal perovskites (see ref 2 for the derivation of layer sequences and corresponding space group symmetries).

Close packed layers within perovskite structures can be classified as either "cubic" (*c*) or "hexagonal" (*h*). Cubic layers lie at the center of an ABC stacking sequence and connect the BO_6 octahedral sites in a corner-sharing manner. Hexagonal layers lie at the center of an ABA stacking sequence and connect BO_6 sites in a face-sharing manner. The relative proportion of hexagonal and cubic layers, in the structures of phases which adopt mixed stacking sequences, can be rationalized with reference to the structural tolerance factor, $t = (r_A + r_O)/\sqrt{2}(r_B + r_O)$, where r_A, r_B, and r_O are the ionic radii of A, B, and O, respectively. A tolerance factor of unity is the geometrically ideal ratio of the A and B cation radii for the formation of an unstrained cubic (3C) perovskite structure in which the large A-cations are accommodated in 12-coordinate sites within a three-dimensional network of corner-sharing BO_6 octahedra. Small deviations of the tolerance factor below unity are accommodated by cooperative twisting and tilting distortions of the BO_6 octahedra in which the B−O−B bond angle is reduced below 180° to accommodate small A-site cations.

Deviations of the tolerance factor above unity drive structures to incorporate hexagonal close packed layers to expand the

[†] University of Antwerp.
[‡] University of Oxford.

(1) Cooper, S. L.; Egami, T.; Goodenough, J. B.; Zhou, J.-S. *Localized to itinerant electronic transition in perovskite oxides*. Springer-Velang: Berlin, Heidelburg, New York, 2001.

(2) Belov, N. V. *Structure of Ionic Crystals and Metallic Phases*; Academy of Science (USSR): Moscow, 1947.

10.1021/ja903216d CCC: $40.75

A-cation sites, introducing face-sharing links into the BO_6 sublattice. Thus the ratio of cubic to hexagonal layers, and therefore the ratio of corner and face-sharing links between BO_6 octahedra, in hexagonal perovskites is dependent on the size of the tolerance factor[3] as demonstrated by the structural progression of the group two $AMnO_3$ manganates. $CaMnO_3$ ($t = 0.987$) adopts a distorted cubic perovskite structure (all corner-sharing);[4] $SrMnO_3$ ($t = 1.033$) adopts a 4H structure (1:1 corner/face-sharing);[5] $BaMnO_3$ ($t = 1.089$) adopts a 2H structure (all face-sharing).[6]

In addition to simple isovalent cation substitutions, the tolerance factor can also be adjusted by the introduction of anion deficiency. Lowering the anion concentration leads to a reduction of the B-cation oxidation state which is associated with an expansion in the B-cation radius which consequently lowers the tolerance factor. There are a number of different ways in which anion vacancies can be incorporated within hexagonal perovskite structures. The exact arrangement adopted is strongly influenced by the transition metal(s) present. For example in the $BaMnO_{3-x}$ series the oxide ion vacancies were initially assumed to be located in the cubic layers giving them an overall formula of $BaO_{2.5}$. It was proposed that there is an approximate relationship between the relative proportions of hexagonal and cubic layers and the overall stoichiometry of a phase, expressed by the formula $x = (0.5c)/(h + c)$, where x is the oxygen non-stoichiometry and c and h are the respective numbers of cubic and hexagonal layers in a repeat unit. Indeed, stacking of the cubic $BO_{2.5}$ layers and BaO_3 hexagonal layers gives the proposed relationship between composition and structure.[7−10] However neutron powder diffraction data demonstrated unambiguously that the oxygen deficiency in the 15R $(chhhh)_3$, 8H $(chhh)_2$, 6H $(chhhch)$, 10H $(chhch)_2$, and 4H $(chch)$ $BaMnO_{3-x}$ perovskites does not obey the simple $x = (0.5c)/(h + c)$ equation[11] and that the anion vacancies in these phases are located predominantly in the hexagonal layers.[11,12] The strong preference for locating anion vacancies in the hexagonal layers of $BaMnO_{3-x}$ phases is supported by the observation that oxide ions located in cubic layers have shorter Ba−O distances than those in hexagonal layers, leading to a larger loss of lattice energy when anions are removed from cubic layers.[11]

Considering this apparent strong preference for manganese containing hexagonal perovskites to accommodate anion vacancies within hexagonal layers, the idealized 4H-$AMnO_2$ structure would be expected to have an ordered alternation of the hexagonal AO layers and cubic AO_3 layers and consist of corner-sharing Mn_2O_7 tetrahedral groups. Neutron powder diffraction data collected from $Ba_{0.5}Sr_{0.5}MnO_{2+x}$ reveal that the oxygen vacancies are randomly distributed over the hexagonal and cubic layers of this phase, albeit with a slight preference for locating anion vacancies in the hexagonal layers. The existence of Mn_2O_7 (two corner-sharing tetrahedra) and Mn_2O_6 (two edge-sharing tetrahedra) groups was proposed based on the analysis of possible local coordination environments of the manganese atoms and crystal chemistry considerations.[13]

In this contribution we demonstrate that in the structure of 4H-$BaMnO_{2+x}$ (prepared by topotactic reduction of 4H-$BaMnO_{3-x}$) the oxygen atoms and anion vacancies are fully ordered resulting in an orthorhombic superstructure. We confirm the existence of the proposed Mn_2O_7 and Mn_2O_6 groups and derive the compositions and structures of novel anion deficient close-packed BaO_{3-x} layers, which can be used in the future for building new types of close-packed anion deficient ABO_{3-x} perovskites.

Experimental Section

Preparation of 4H-$BaMnO_{3-x}$. 4H-$BaMnO_{3-x}$ was prepared by a standard ceramic route. Suitable quantities of $BaCO_3$ (99.997%, Alfa Aesar) and MnO_2 (99.999%, Alfa Aesar) were thoroughly mixed in an agate pestle and mortar before being heated at 900 °C in air to decompose the carbonates. The resulting black powders were reground and pressed into 13 mm pellets under 5 tonnes of pressure before being heated for two periods of 2 days at 1300 °C under flowing argon. Samples were reground and pressed into pellets between heating periods. After the final heating period, samples were cooled at 10 °C per minute to room temperature under argon. X-ray powder diffraction data collected from samples could be indexed on the basis of a hexagonal unit cell with lattice parameters consistent with previous reports.[12]

Reduction of 4H-$BaMnO_{3-x}$. Samples of 4H-$BaMnO_{3-x}$ (5 g) were combined with a double stoichiometric excess of LiH in an argon filled glove box (O_2, H_2O < 1ppm). The resulting mixture was heated at 350°C for two periods of 2 days (with intermediate regrinding) within a "venting" apparatus, described previously,[14] due to the hazards associated with the formation of hydrogen gas when using LiH as a reducing agent.[13] After reaction the samples were washed with dry methanol to remove the lithium containing species (LiH, Li_2O) before being dried thoroughly under vacuum. Due to the apparent strong affinity of the product for methanol, samples were heated at 150°C under vacuum for 2 h to complete the drying process.

Characterization. X-ray powder diffraction (XRPD) data were collected using a Panalytical X'pert diffractometer incorporating an X'celerator position sensitive detector (monochromatic $CuK_{\alpha 1}$ radiation), equipped with an air-sensitive cell. The structure solution and the Rietveld refinement from XRPD data were performed using the JANA2000 program package.[15] Samples for the electron microscopy investigation were prepared by crushing the powder sample in ethanol and depositing it on a holey carbon grid. Electron diffraction (ED) studies were performed using a Philips CM20 microscope. Neutron powder diffraction data were collected using the POLARIS instrument at the ISIS neutron source, Rutherford Appleton Laboratory, UK. Data were collected from a sample contained in a vanadium can which had been sealed under argon with an indium washer in the case of the 2 and 298 K data sets or a copper gasket in the case of the 373 K data set. Rietveld structural refinements were performed against the neutron powder diffraction data utilizing the GSAS suite of programs.[16] Average manganese oxidation states were determined by dissolving samples in HCl containing an excess of KI and titrating the liberated I_2 with $Na_2S_2O_3$. Magnetization data were collected in the temperature

(3) Darriet, J.; Subramanian, M. A. *J. Mater. Chem.* **1995**, *5*, 543–552.
(4) Poeppelmeier, K. R.; Leonowicz, M. E.; Scanlon, J. C.; Longo, J. M.; Yelon, W. B. *J. Solid State Chem.* **1982**, *45*, 71–79.
(5) Battle, P. D.; Gibb, T. C.; Jones, C. W. *J. Solid State Chem.* **1988**, *74*, 60–66.
(6) Cussen, E. J.; Battle, P. D. *Chem. Mater.* **2000**, *12*, 831–838.
(7) Gonzalez-Calbet, J. M.; Parras, M.; Alonso, J. M.; Vallet-Regi, M. *J. Solid State Chem.* **1993**, *106*, 99–110.
(8) Gonzalez-Calbet, J. M.; Parras, M.; Alonso, J. M.; Vallet-Regi, M. *J. Solid State Chem.* **1994**, *111*, 202–207.
(9) Parras, M.; Alonso, J. M.; Gonzalez-Calbet, J. M.; Vallet-Regi, M. *J. Solid State Chem.* **1995**, *117*, 21–29.
(10) Parras, M.; Gonzalez-Calbet, J. M.; Alonso, J. M.; Vallet-Regi, M. *J. Solid State Chem.* **1994**, *113*, 78–87.
(11) Adkin, J. J.; Hayward, M. A. *Chem. Mater.* **2007**, *19*, 755–762.
(12) Adkin, J. J.; Hayward, M. A. *J. Solid State Chem.* **2006**, *179*, 70–76.
(13) Adkin, J. J.; Hayward, M. A. *Inorg. Chem.* **2008**, *47*, 10959–10964.
(14) O'Malley, M.; Lockett, M. A.; Hayward, M. A. *J. Solid State Chem.* **2007**, *180*, 2851–2858.
(15) Petríček, V.; Dušek, M. *The Crystallographic Computing System JANA2000*; Institute of Physics AVCR: Praha, Czech Republic, 2000.
(16) Larson, A. C.; Von Dreele, R. B. *General Structure Analysis System*; Los Alamos National Laboratory Report LAUR 86−748: 2000.

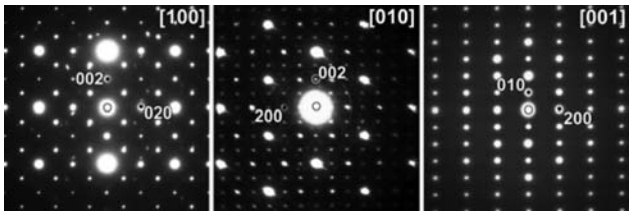

Figure 1. Electron diffraction patterns along the main zones [100], [010], and [001] of 4H-$BaMnO_{2+x}$.

range $5 < T/K < 400$ from powdered samples in an applied field of 1000 Oe using a Quantum Design MPMS SQUID magnetometer.

Results

Unit Cell and Space Group Determination. The crystallographic unit cell of 4H-$BaMnO_{2+x}$ was determined using electron diffraction. Several tilt series were taken to reconstruct the reciprocal lattice, of which the diffraction patterns of the three main zones are shown in Figure 1. All ED patterns could be indexed on the basis of an orthorhombic unit cell with the parameters $a \approx 10.4$ Å, $b \approx 9.4$ Å, $c \approx 11.2$ Å. The reflection conditions derived from the ED patterns are *hkl*: no conditions; 0*kl*: $k + l = 2n$; *h*0*l*: no conditions; *hk*0: $h = 2n$; *h*00: $h = 2n$; 0*k*0: $k = 2n$; 00*l*: $l = 2n$. These reflection conditions correspond to the extinction symbol *Pn_a*, leaving two possible space groups *Pnma* and $Pn2_1a$. The centrosymmetric space group *Pnma* will be used for further structure determination from X-ray and neutron powder diffraction data. The occurrence of the forbidden reflections 00*l*: $l = 2n + 1$ on the [100] ED pattern and of *h*00: $h = 2n + 1$ and 0*k*0: $k = 2n + 1$ on the [001] ED pattern (Figure 1) is due to double diffraction, as is proven by the absence of these reflections on the other main zone ED patterns of Figure 1. The lattice parameters determined from the ED data allow the complete indexation of the X-ray powder diffraction data from which accurate values of the lattice parameters ($a = 10.3184(5)$ Å, $b = 9.4582(2)$ Å, $c = 11.2799(5)$ Å) could be refined.

Structure Determination. The oxygen content of the reduced product was determined by iodometric titration to be $BaMnO_{2.06(1)}$, consistent with the formulation $BaMnO_{2+x}$. By analogy to the previously reported phase 4H−$Ba_{0.5}Sr_{0.5}MnO_{2+x}$[13] it is reasonable to assume the low temperature reduction of 4H-$BaMnO_{3-x}$ is topotactic. That is to say the deintercalation of oxide ions does not significantly affect the cation sublattice. However in contrast to 4H-$Ba_{0.5}Sr_{0.5}MnO_{3-x}$ the reduction of 4H-$BaMnO_{3-x}$ is accompanied by a lowering of the crystal symmetry from hexagonal ($P6_3/mmc$) to orthorhombic (*Pnma*). This symmetry lowering is taken to be an indication that the anion vacancies in 4H-$BaMnO_{2+x}$ adopt an ordered arrangement.

The lattice vectors of the hexagonal unit cell of 4H-$BaMnO_{3-x}$ are related to the lattice vectors of the orthorhombic unit cell by the transformation matrix:

$$\begin{bmatrix} 1 & 2 & 0 \\ 0 & 0 & 1 \\ 2 & 0 & 0 \end{bmatrix}$$

Applying this transformation to the atomic coordinates of hexagonal 4H-$BaMnO_{3-x}$ atomic positions for the orthorhombic supercell were calculated. *Pnma* symmetry was implemented by a subsequent translation of the origin over the vector:

$$\begin{bmatrix} 0.25 \\ 0 \\ 0.125 \end{bmatrix}$$

These cation positions were used as an initial model for the structural refinement. The oxygen atoms were localized using several difference Fourier map−refinement cycles. The atomic coordinates of all atoms were subsequently refined using the XRPD data. The refinement resulted in a good agreement between the experimental and calculated XRPD profiles with $R_I = 0.038$ and $R_P = 0.031$.

Given the low sensitivity of X-ray diffraction data to the location of light atoms in the presence of much heavier elements, the results of the XRPD refinement were used as a starting point for further refinement using neutron powder diffraction (NPD) data. The NPD patterns of 4H-$BaMnO_{2+x}$ measured at $T = 2$ and 298 K exhibit diffraction features which are absent in the data collected at $T = 373$ K (Figure 2). The intensity of these features increases with decreasing temperature suggesting they are of magnetic origin. Given the presence of these magnetic diffraction features, the refinement of the crystal structure was performed using neutron diffraction data collected at $T = 373$ K, which lies above the magnetic ordering temperature, as discussed later. To reduce correlations atomic displacement parameters were constrained by element. The refinement against data from all three detector banks (35°, 90°, and 145°) converged readily. The crystallographic data and atomic coordinates of 4H-$BaMnO_{2+x}$ are summarized in Table 1. The most relevant interatomic distances and selected bond angles are listed in Tables 2 and 3, respectively. Observed, calculated, and difference plots from the structural refinement against the data collected using the 35° detector bank are shown in Figure 2.

This structural data were used to simulate high resolution transmission electron microscopy images, such as shown in Figure 3, which are in excellent agreement with the experimental images. The simulation put inside the HRTEM image of Figure 3 was made at a focus value of $f = -280$ Å and a thickness of $t = 60$ Å.

Magnetic Characterization. Magnetization data collected from 4H-$BaMnO_{2+x}$ are shown in Figure 4. It can be seen that the zero-field cooled and field cooled data diverge below $T \approx 350$ K and the data cannot be fitted to the Curie−Weiss law over any significant temperature range. When combined with the additional diffraction features observed in the neutron diffraction data collected at 298 and 2 K, the magnetization data are consistent with the onset of magnetic order at 350 K.

The magnetic diffraction features observed in the neutron diffraction data can be indexed on the crystallographic unit cell with a $\mathbf{k} = 0$ propagation vector. The magnetic structures of $BaMnO_{3-x}$ phases all have the ordered magnetic moments of the manganese centers directed perpendicular to the crystallographic stacking direction.[11] The lack of any strong magnetic *h*0*l* reflections in the data collected from 4H-$BaMnO_{2+x}$ is consistent with an analogous situation in which the spins are aligned within the *ac* plane. After testing all eight possible magnetic space groups derived from the structural space group *Pnma*, the magnetic space group *Pn′ma* was found to support a simple magnetic model in which all Mn−O−Mn links are antiferromagnetically coupled and the magnetic moments of all the manganese centers lie parallel or antiparallel to the *c* lattice vector. This model was refined against the data collected at 298 and 2 K achieving good agreement in both cases ($\chi^2 = 2.03$, $T = 298$ K; $\chi^2 = 3.13$, $T = 2$ K). Moments of $2.78(4)\mu_B$ and

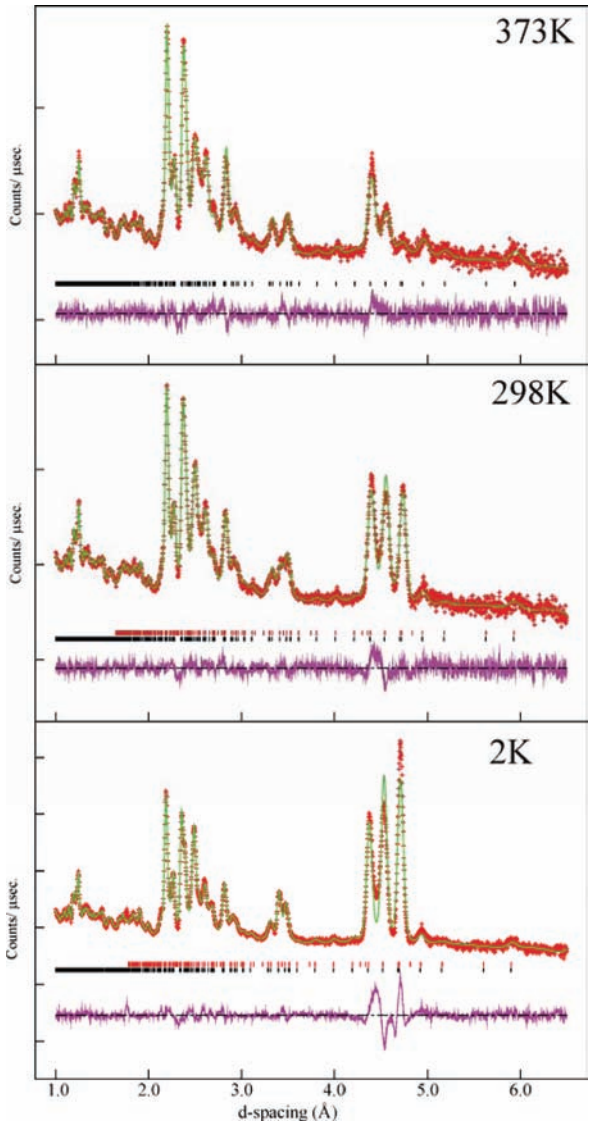

Figure 2. Observed, calculated, and difference plots from the Rietveld refinements of 4H-BaMnO$_{2+x}$ against neutron powder diffraction data collected from the 35° detector bank at 373, 298, and 2 K.

Table 1. Positional and Atomic Displacement Parameters of 4H-BaMnO$_{2+x}$ at 373 K[a]

atom	position	*x*	*y*	*z*	U_{iso} (Å^3)
Ba(1)	*8d*	0.2292(3)	0.4782(2)	0.6191(3)	0.0106(5)
Ba(2)	*4c*	0.0716(4)	0.25	0.8814(4)	0.0106(5)
Ba(3)	*4c*	0.5763(5)	0.25	0.1324(4)	0.0106(5)
Mn(1)	*8d*	0.1096(3)	0.8878(3)	0.8629(3)	0.0055(4)
Mn(2)	*8d*	0.9179(3)	0.1056(3)	0.6340(3)	0.0055(4)
O(1)	*4c*	0.4400(4)	0.75	0.1457(3)	0.0179(4)
O(2)	*8d*	0.7560(3)	0.5460(2)	0.1153(3)	0.0179(4)
O(3)	*4b*	0.5	0.5	0	0.0179(4)
O(4)	*4c*	0.8444(4)	0.25	0.9985(5)	0.0179(4)
O(5)	*8d*	0.5361(2)	0.4875(2)	0.2812(2)	0.0179(4)
O(6)	*4c*	0.3185(4)	0.25	0.2289(4)	0.0179(4)

[a] 4H-BaMnO$_2$ at 373 K, space group: *Pnma*. Lattice parameters: a = 10.375(2) Å, b = 9.466(2) Å, c = 11.276(3) Å, volume = 1107.3(8)Å^3. χ^2 = 1.94, wRp = 1.00%, Rp = 1.68%.

4.47(3)μ_B per manganese center were refined from the data collected at 298 and 2 K, respectively, consistent with the transition temperature 350 K determined from the susceptibility measurements. The weak residual intensity at ~4.5 Å in the data collected at 2 K suggests there is a small amount of short range order present at low temperature which is not accounted for by the magnetic model. Complete details of the structural and magnetic refinements performed against the 2 and 298 K data are given in the Supporting Information. Observed, calculated, and difference plots from these structural refinements are shown in Figure 2.

Table 2. Selected Bond Lengths of 4H-BaMnO$_{2+x}$ at 373 K

cation	anion	bond length (Å)
Mn(1)	O(2)	2.061(4)
	O(4)	2.091(5)
	O(5)	2.006(4)
	O(6)	2.131(5)
Mn(2)	O(1)	2.015(4)
	O(2)	1.902(4)
	O(3)	2.002(3)
	O(5)	2.057(4)
Ba(1)	O(1)	2.799(4)
	O(2)	2.734(5)
	O(2)	3.007(5)
	O(3)	2.739(3)
	O(4)	2.802(4)
	O(5)	3.320(4)
	O(5)	2.701(4)
	O(6)	2.898(3)
Ba(2)	O(1)	2.660(6)
	O(2)×2	2.632(4)
	O(4)	2.702(6)
	O(5)×2	2.949(3)
Ba(3)	O(1)	3.140(6)
	O(2)×2	3.371(4)
	O(3)×2	2.908(3)
	O(4)	3.165(7)
	O(5)×2	2.836(3)
	O(6)×2	2.960(7)

Table 3. O−Mn−O Bond Angles of 4H-BaMnO$_{2+x}$ at 373 K

atoms	bond angle (deg)	atoms	bond angle (deg)
O(2)−Mn(1)−O(4)	102.19(1)	O(1)−Mn(2)−O(2)	154.485(5)
O(2)−Mn(1)−O(5)	102.86(2)	O(1)−Mn(2)−O(3)	94.44(1)
O(2)−Mn(1)−O(6)	107.04(2)	O(1)−Mn(2)−O(5)	98.43(1)
O(4)−Mn(1)−O(5)	143.922(5)	O(2)−Mn(2)−O(3)	99.85(1)
O(4)−Mn(1)−O(6)	93.91(2)	O(2)−Mn(2)−O(5)	98.508(8)
O(5)−Mn(1)−O(6)	103.04(2)	O(3)−Mn(2)−O(5)	103.85(2)

Discussion

Crystal Structure. The refined structure of 4H-BaMnO$_{2+x}$ (Figure 5, Table 1) consists of an ordered arrangement of anion vacancies within the original 4H-BaMnO$_{3-x}$ host structure, indicating a simple topotactic reaction has occurred. The structural tolerance factor of this phase (t = 1.01, calculated

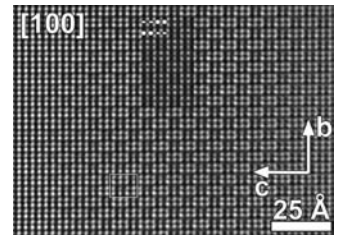

Figure 3. High resolution transmission electron microscopy image along [100] of 4H-BaMnO$_{2+x}$. The black dots are positioned at the projections of the Ba-columns. The location of the center of a few Mn_2O_7 groups is indicated by a white dot and that of Mn_2O_6 groups by a white dash. A projected unit cell is outlined using a white rectangle.

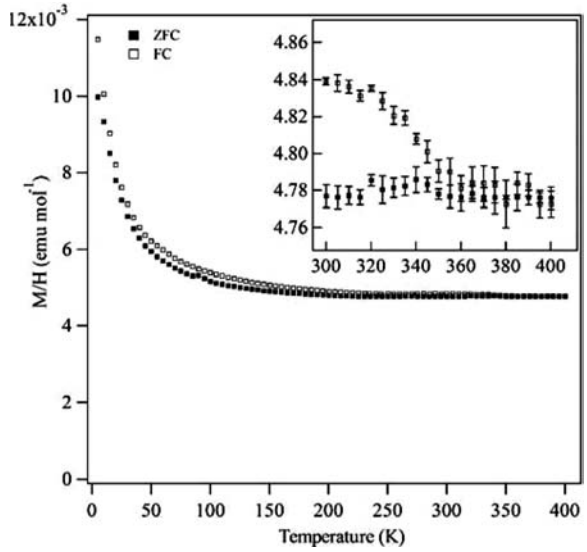

Figure 4. Zero-field cooled and field cooled magnetization data collected from 4H-$BaMnO_{2+x}$. Inset shows divergence at $T \sim 350$ K assigned as the antiferromagnetic ordering temperature.

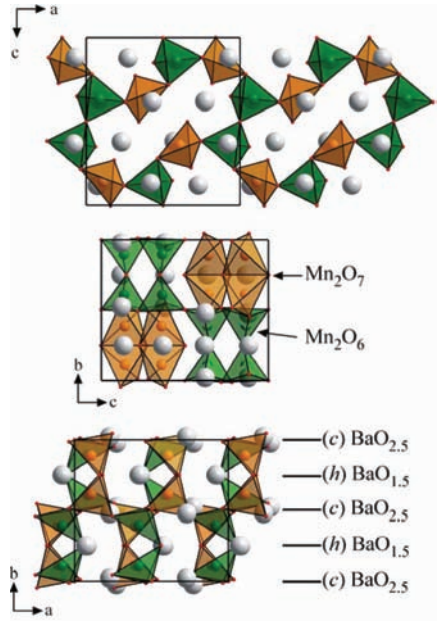

Figure 5. Projections of the 4H-$BaMnO_{2+x}$ structure along the [010], [100], and [001] axes. The tetrahedra contain Mn at their centers and oxygen at the corners; Mn_2O_7 units are yellow, Mn_2O_6 units green. Barium atoms are represented by gray spheres.

from the structural data) is much reduced from the value 1.055 for 4H-$BaMnO_{2.65}$.[12] This low value is now consistent with a cubic (3C) structure, rather than the 4H structure observed, indicating that the relationship between composition and structure which usually holds for perovskite phases has been broken. The large decrease in the tolerance factor of 4H-$BaMnO_{2+x}$ relative to 4H-$BaMnO_{3-x}$ is driven by the extension of the average Mn−O bond length. This extension also leads to a buckling of the Mn−O lattice as observed by the decrease in the average Mn−O−Mn bond angle from 180° to 145.6(2)°.

The ordered removal of oxide ions from the structure of 4H-$BaMnO_{3-x}$ to form 4H-$BaMnO_{2+x}$ leads to the conversion of Mn_2O_{9-x} groups into Mn_2O_7 and Mn_2O_6 groups which share corners to form the overall manganese−oxygen framework of

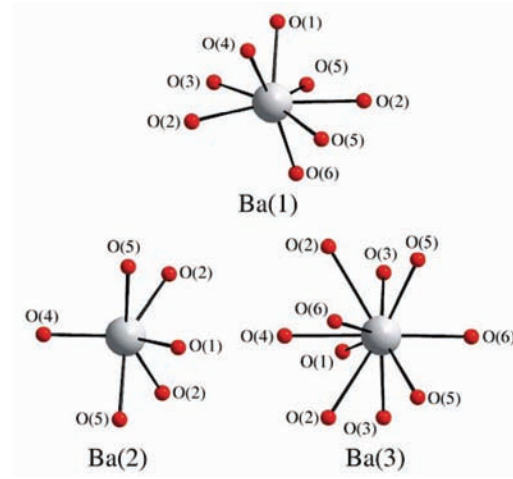

Figure 6. Coordination environments of the barium atoms in the 4H-$BaMnO_{2+x}$ structure.

the phase. It can be seen from Figure 5 that the Mn_2O_7 groups (site Mn(2)) consist of distorted corner-sharing MnO_4 tetrahedra formed by the removal of two oxide ions from the hexagonal layer. By comparison the Mn_2O_6 units (site Mn(1)) consist of distorted edge-sharing tetrahedra formed by the removal of oxide ions from the cubic layers and hexagonal layers. The average bond lengths for the two tetrahedrally coordinated manganese positions are 2.072 Å for Mn(1) and 1.994 Å for Mn(2) (Table 2). These distances are comparable to the Mn−O distances in other Mn(II)O_4 tetrahedra, such as those in Mn_3O_4 (2.078 Å),[17] Ba_2MnO_3 (2.000 and 2.080 Å),[18] and $K_2Mn_2O_3$ (2.068 Å).[19] The O−Mn−O tetrahedral bond angles (Table 3) deviate significantly from the ideal ∠O−Mn−O = 109.47° tetrahedral bond angle. This can be seen as a reflection of the limited structural relaxation which is possible on reduction under low temperature reaction conditions. The barium atoms in the 4H-$BaMnO_{2+x}$ structure have relatively low coordination numbers CN = 6, 8, and 10. CN = 6 might appear to be too small for the large barium cations, especially in comparison with the CN = 12 in the perovskite structure. However, the average Ba−O bond distance for the 6-fold coordinated Ba(2) atom (2.754 Å) is similar to the Ba−O distance for the octahedrally coordinated barium atoms in the NaCl-type BaO structure (2.767 Å).[20] The oxygen coordination of the barium atoms in 4H-$BaMnO_{2+x}$ is shown in Figure 6.

The occurrence of Mn_2O_7 and Mn_2O_6 groups was also suggested for 4H-$Ba_{0.5}Sr_{0.5}MnO_{2+x}$ which was prepared by the reduction of 4H-$Ba_{0.5}Sr_{0.5}MnO_{3-x}$.[13] A significant difference between the structures of the two phases is that the anion vacancies in 4H-$Ba_{0.5}Sr_{0.5}MnO_{2+x}$ are disordered. However the concentration of anion vacancies in the hexagonal and cubic layers in the structure of 4H-$Ba_{0.5}Sr_{0.5}MnO_{2+x}$ is consistent with the presence of the same Mn_2O_7 and Mn_2O_6 building units seen in 4H-$BaMnO_{2+x}$ suggesting the same manganese local coordinations are present in both phases.

Magnetic Structure. The magnetic structure refined for 4H-$BaMnO_{2+x}$ (Figure 7) is consistent with simple antiferromagnetic superexchange between d^5 centers. The observed ordered mo-

(17) Satomi, K. *J. Phys. Soc. Jpn.* **1961**, *16*, 258–265.
(18) Sander, K.; Mueller-Buschbaum, H. *Z. Anorg. Allg. Chem.* **1981**, *47*, 52–56.
(19) Seipp, E.; Hoppe, R. *Z. Anorg. Allg. Chem.* **1985**, *530*, 117–126.
(20) Burgers, W. G. *Z. Phys.* **1933**, *80*, 352–360.

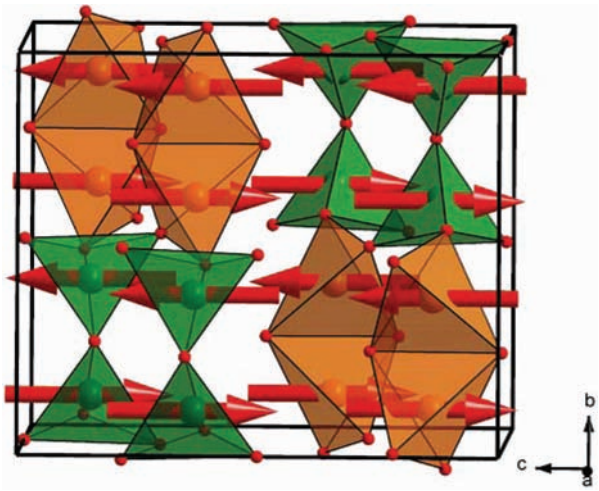

Figure 7. Refined magnetic structure of 4H-$BaMnO_{2+x}$. Ordered moment at 2 K = 4.47(3)μ_B per manganese.

ment of 4.47(3)μ_B per manganese at 2 K represents ~90% of the moment expected for an $s = {}^5/_2$ center and is considerably larger than that observed for 4H-$Ba_{0.5}Sr_{0.5}MnO_{2+x}$ (3.73(3)μ_B)[13] presumably due to the structural disorder observed in the latter phase, although both phases exhibit similar magnetic ordering temperatures (4H-$BaMnO_{2+x}$: 350 K, 4H-$Ba_{0.5}Sr_{0.5}MnO_{2+x}$ 355 K[13]). The relatively high magnetic ordering temperature observed is not unexpected for a d^5 system as discussed previously.[13]

Anion Vacancies in Close Packed Structures. The structures of anion vacancy ordered perovskites can be analyzed by considering the stacking of anion deficient AO_{3-x} close packed layers (Figure 8a). Anderson *et al.*[21] observed that a large number of anion-vacancy ordered cubic (3C) perovskites have a unique AO_{3-x} close packed layer, which when stacked in an ABCA manner generates the overall structural lattice. Furthermore they observed that apparently dissimilar anion deficient structures can be described by the stacking of a common AO_{3-x} layer. For example the brownmillerite structure consists of four- and six-coordinate B-cations, while the structure of $Ca_2Mn_2O_5$ has five-coordinate manganese centers. Both structures can be generated by the stacking of the same anion deficient $AO_{2.5}$ layer (Figure 8b).

The description of anion deficient hexagonal perovskites is more intuitive. For example, anion vacancies are often accommodated by the formation of AO_2 layers (Figure 8c, 8d). These anion deficient layers can be formed by the removal of oxide ions from stoichiometric AO_3 layers in a topotactic manner. Such a process converts 2H-$BaNiO_3$ into 2H-$BaNiO_2$,[22] the structure of which can be generated by the simple stacking of vacancy ordered AO_2 layers (Figure 8c) resulting in a square planar coordination for nickel. Alternatively AO_2 layers can be generated by the replacement of a "triangle" of three anions with a single anion (Figure 8d). This converts a BO_6 octahedral site into a BO_4 tetrahedral site. Hexagonal AO_2 layers "accommodate" the anion vacancies in $BaFeO_{2.8}$,[23] forming bilayers

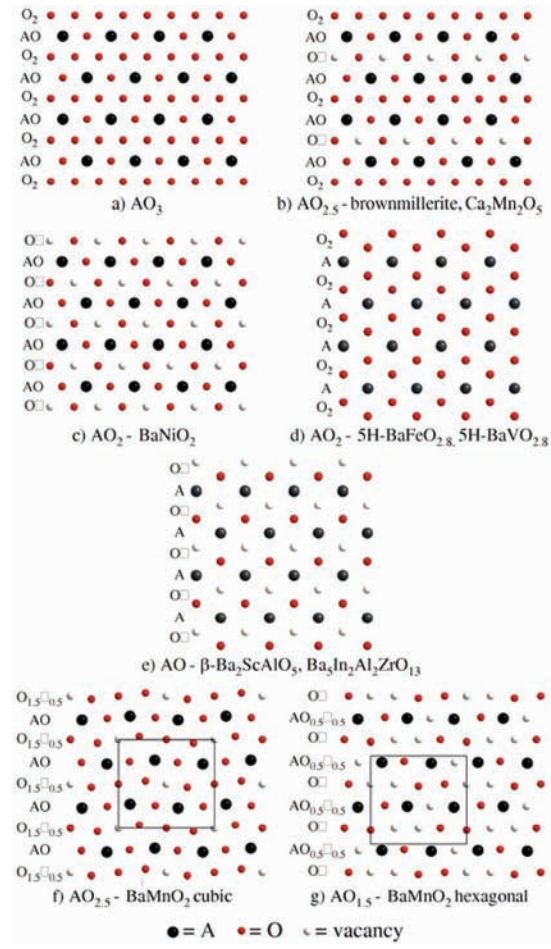

Figure 8. Arrangement of atoms in the (a) AO_3 close packed layers, (b) $AO_{2.5}$ layers present in the brownmillerite and $Ca_2Mn_2O_5$ structures, (c) AO_2 layers present in $BaNiO_2$, and (d) 5H-$BaFeO_{2.8}$ and 5H-$BaVO_{2.8}$, (e) AO layers present in β-Ba_2ScAlO_5 and $Ba_5In_2Al_2ZrO_{13}$. The structure of 4H-$BaMnO_{2+x}$ is formed from the alternate stacking of (f) cubic $AO_{2.5}$ layers and (g) hexagonal $AO_{1.5}$ layers.

of BO_4 tetrahedra which are apex-linked, while in $BaVO_{2.8}$[24] cubic AO_2 layers "accommodate" the anion vacancies, giving bilayers of unlinked BO_4 tetrahedra.

Further removing half of the oxygen atoms in an ordered manner from such an AO_2 layer produces an AO layer (Figure 8e). Replacement of a hexagonally stacked AO_3 layer with an AO layer of this type converts a B_2O_9 pair of face-sharing BO_6 octahedra into a B_2O_7 pair of corner-sharing BO_4 tetrahedra, as observed in the structure of β-Ba_2ScAlO_5 and $Ba_5In_2Al_2ZrO_{13}$.[25,26]

Despite both AO_2 layers described above, and a combination of AO_3 and AO layers, having the correct stoichiometry, the anion vacancies present in the structure of 4H-$BaMnO_{2+x}$ are accommodated in a different way. The structure of 4H-$BaMnO_{2+x}$ is formed by the alternate stacking of $AO_{1.5}$ and $AO_{2.5}$ layers (Figure 8f, 8g) resulting in an ordered arrangement of edge- and corner-linked MnO_4 tetrahedra (Figure 5). The complex anion vacancy arrangement adopted by 4H-$BaMnO_{2+x}$ can be rationalized by considering the coordination preferences of both the barium and manganese cations in a manner which

(21) Anderson, M. T.; Vaughey, J. T.; Poeppelmeier, K. R. *Chem. Mater.* **1993**, *5*, 151–165.
(22) Krischner, H.; Torkar, K.; Kolbesen, B. O. *J. Solid State Chem.* **1971**, *3*, 349–357.
(23) Delattre, J. L.; Stacy, A. M.; Siegrist, T. *J. Solid State Chem.* **2004**, *177*, 928–935.
(24) Liu, G.; Greedan, J. E. *J. Solid State Chem.* **1994**, *110*, 274–289.
(25) Shpanchenko, R. V.; Abakumov, A. M.; Antipov, E. V.; Kovba, L. M. *J. Alloys Compd.* **1994**, *206*, 185–188.
(26) Shpanchenko, R. V.; Antipov, E. V.; Lykova, L. N.; Kovba, L. M. *Vestn. Mosk. Univ. Ser. Khim.* **1990**, *31*, 555.

has been successful for the analysis of other topotactically reduced manganates.[13,25] As noted above the AO_2 anion deficient layers present in the structure of $BaNiO_2$ can be stacked to form phases of ABO_2 stoichiometry in which the B-cations adopt a square planar coordination. If a different stacking arrangement is adopted a 4H structure of ABO_2 stoichiometry can be produced with contains corner-linked B_2O_6 groups of edge-sharing BO_4 tetrahedra. However, as noted above, due to differences in barium−oxygen bond lengths, there is an energetic advantage in locating anion vacancies in the hexagonal layers of $BaMnO_{3-x}$ phases so this ordered arrangement, with equal numbers of vacancies in the hexagonal and cubic layers, is not adopted. Another candidate 4H-ABO_2 structure can be generated by stacking cubic AO_3 layers with hexagonal AO layers. This arrangement would benefit from the energetic advantage of locating all the anion vacancies in the hexagonal layers.

However, in 4H-$BaMnO_{2+x}$ the stacking sequence of the BaO_3 and BaO layers cannot be realized because in the Mn_2O_7 group of corner-linked tetrahedra the bond from the Mn atom to the O atom forming the common vertex of two tetrahedra is directed perpendicular to the close packed layers. Assuming the average separation between the close packed BaO_3 and BaO layers to be ∼2.4 Å, this Mn−O interatomic distance should be as short as ∼1.7−1.8 Å, not appropriate for the large Mn^{2+} cations.

The structure adopted by 4H-$BaMnO_{2+x}$ appears to be a compromise in which 75% of the anion vacancies are located in the hexagonal layers and 25% in the cubic layers. The arrangement of the vacant sites in the hexagonal layers leads to the formation of two distinct barium coordination sites, a 6-coordinate site, and a 10-coordinate site. The formation of two distinct barium sites allows the hexagonal layers to relax, shortening the Ba−O contacts to the 6-coordinate site while lengthening the Ba−O contacts to the 10-coordinate sites. This distortion allows the coordination preferences of all the cations in the structure to be satisfied and leads to a net gain in the lattice energy.

In conclusion, it is clear that the topotactic reduction of hexagonal perovskites allows the coupling between the tolerance factor and structure, which is usually rigidly followed by perovskite materials, to be broken and novel B−O−B transition metal−oxygen networks to be formed. Given the strong dependence of magnetic exchange coupling on B−O−B bond angles, the ability to prepare new metal−oxygen networks potentially offers access to a large number of new magnetic and electronic materials by the topotactic reduction of other hexagonal perovskite phases.

Acknowledgment. We thank the R. Smith for assistance collecting the neutron diffraction data. Experiments at the ISIS Pulsed Neutron and Muon Source were supported by a beamtime allocation from the Science and Technology Facilities Council. A.M.A. is grateful for support by the Russian Foundation of Basic Research (RFBR Grants 07-03-00664-a, 06-03-90168-a). The authors acknowledge financial support from the European Union under the Framework 6 program under a contract for an Integrated Infrastructure Initiative. Reference 026019 ESTEEM.

Supporting Information Available: Details of the nuclear and magnetic structures of 4H-$BaMnO_{2+x}$ at 298 and 2 K.This material is available free of charge via the Internet at http://pubs.acs.org.

JA903216D